Journal of Materials Science & Technology 132 (2023) 110–118

Contents lists available at ScienceDirect

Journal of Materials Science & Technology

journal homepage: www.elsevier.com/locate/jmst

Research Article

Deformation mechanisms for a new medium-Mn steel with 1.1 GPa yield strength and 50% uniform elongation

Wei Wang[a], Yanke Liu[a,b], Zihan Zhang[a,b], Muxin Yang[a], Lingling Zhou[a,b], Jing Wang[a], Ping Jiang[a], Fuping Yuan[a,b,*], Xiaolei Wu[a,b]

[a] State Key Laboratory of Nonlinear Mechanics, Institute of Mechanics, Chinese Academy of Sciences, Beijing 100190, China
[b] School of Engineering Sciences, University of Chinese Academy of Sciences, Beijing 100049, China

ARTICLE INFO

Article history:
Received 25 March 2022
Revised 12 May 2022
Accepted 29 May 2022
Available online 1 July 2022

Keywords:
Medium-Mn steel
Strain hardening
Ductility
Martensite transformation
Strain gradient
Mobile dislocations

ABSTRACT

A new medium-Mn steel was designed to achieve unprecedented tensile properties, with a yield strength beyond 1.1 GPa and a uniform elongation over 50%. The tensile behavior shows a heterogeneous deformation feature, which displays a yield drop followed by a large Lüders band strain and several Portevin-Le Châtelier bands. Multiple strain hardening mechanisms for excellent tensile properties were revealed. Firstly, non-uniform martensite transformation occurs only within a localized deformation band, and initiation and propagation of every localized deformation band need only a small amount of martensite transformation, which can provide a persistent and complete transformation-induced-plasticity effect during a large strain range. Secondly, geometrically necessary dislocations induced from macroscopic strain gradient at the front of localized deformation band and microscopic strain gradient among various phases provide strong heter-deformation-induced hardening. Lastly, martensite formed by displacive shear transformation can inherently generate a high density of mobile screw dislocations, and interstitial C atoms segregated at phase boundaries and enriched in austenite play a vital role in the dislocation multiplication due to the dynamic strain aging effect, and these two effects provide a high density of mobile dislocations for strong strain hardening.

1. Introduction

Safety issues, fuel efficiency, and emission reduction are the important motivations for the development of advanced high-strength steel (AHSS) with both high strength and large ductility in the automotive industry for decades [1–7]. However, strength and ductility are mutually exclusive in general, and the elevation of yield strength up to 1 GPa is usually accompanied by a substantial loss of tensile uniform elongation [8–10]. The first-generation AHSS can achieve high strength, but the ductility is limited, such as dual-phase steels and complex phase steels [2]. Although the second-generation AHSS has both high strength and high ductility, the high amount of alloying content has raised production costs and created various drawbacks in the production processes, such as high Mn transformation-induced-plasticity (TRIP) [11] and twinning-induced-plasticity (TWIP) steels [12]. The medium-Mn steel (MMS) with Mn content in the range of 4–12wt.% is regarded as the most promising candidate for the third-generation automotive steel due to its excellent mechanical properties and relatively low cost [13–18].

The MMS with α-ferrite and γ-austenite phases and equi-axed ultrafine-grains by cold rolling and subsequent intercritical annealing in a two-phase region, revealed the discontinuous yielding and the Lüders band (LB) in general [19,20], and the Lüders band was commonly thought to be caused by static strain aging [21]. The Portevin-Le Châtelier (PLC) band has also been frequently reported for the MMS [22,23], which was proposed to be caused by dynamic strain aging (DSA) associated with the interactions between mobile dislocations and diffusing solute atoms [24–27]. The strain hardening and ductility of MMS can be primarily attributed to the TRIP effect of the retained austenite, which also is determined by both the phase fraction and the stability of the retained austenite [14]. According to a thermodynamic model [28], the higher intercritical annealing temperature, the more fraction of austenite with less enrichment of austenite stabilizers (such as Mn and C) can result in lower mechanical stability of austenite [29]. The pinning effects of interstitial C atoms on dislocations and interfaces help inhibit grain growth during intercritical annealing process [30], and C seg-

* Corresponding author at: State Key Laboratory of Nonlinear Mechanics, Institute of Mechanics, Chinese Academy of Sciences, Beijing 100190, China.
E-mail address: fpyuan@lnm.imech.ac.cn (F. Yuan).

https://doi.org/10.1016/j.jmst.2022.05.048
1005-0302/

regation at the α/γ phase boundaries will increase yield strength and transform the yielding phenomenon from a continuous behavior to a discontinuous pattern [31]. More recently, Al was added in MMS to optimize austenite stability by suppressing cementite formation [32], and the α-γ two-phase range can also be enlarged by Al, such that the processing window, in terms of intercritical annealing temperature, can be expanded [33,34]. Recent research [35] has shown that an MMS (Fe-7.8Mn-1.65Al-0.11Zr-0.14C, wt.%) exhibits excellent strength-ductility synergy with a yield strength of 1022 MPa and a tensile uniform elongation of 41%. However, this MMS has a certain amount of residual austenite content (~9.6%) after tensile failure, which indicates the TRIP effect has not been completely fulfilled.

For AHSS with GPa-level yield strength, the uniform elongation is far less than 50% in general. In the present study, we developed a new MMS and utilized appropriate severe plastic deformation and intercritical annealing process to achieve superior strength-ductility synergy (1.1 GPa yield strength and 50% uniform elongation), and the corresponding deformation mechanisms were revealed. For high-performance MMS, most research efforts have been focused on the influence of the volume fraction and stability of metastable austenite on the mechanical response. However, plastic deformation and ductility are closely related to mobile dislocation density [36]. Heterogeneous deformation also plays a critical role in uniaxial tensile tests of the investigated MMS, and the yield drop phenomenon is caused by the strong deficiency of initial mobile dislocation. Therefore, two key questions should be answered in order to explain the large uniform elongation: where does the mobile dislocation come from and what are the contributing factors for strain hardening?.

2. Materials and experimental methods

2.1. Materials

The chemical composition of the investigated MMS is Fe-6.7Mn-0.46Al-0.28C (wt.%). The materials were casted using a vacuum induction melting furnace under a pure argon atmosphere and were forged into a rectangular ingot. The ingot was homogenized at 1250 °C for 2 h followed by air cooling, and then hot-forged into a plate with a thickness of 30 mm with a starting temperature of 1180 °C and an ending temperature of 900 °C followed by oil cooling. The plate was annealed at an intercritical temperature of 640 °C for 30 min followed by water quenching, and then was subjected to cold rolling with a thickness reduction of 65%. Finally, the cold-rolled (CR) sheet was intercritically annealed at various temperatures (645, 650, 655, 660 °C) for 30 min followed by water quenching.

2.2. Tensile testing

The plate tensile specimens with dog-bone shape and gage dimensions of 18 mm × 2.5 mm × 1.2 mm, were cut from the annealed sheets with longitudinal axis parallel to the rolling direction. All specimens were mechanically polished prior to tensile tests in order to remove surface irregularities and to guarantee an accurate determination of the cross-sectional area. The uniaxial quasi-static tensile tests were carried out using an MTS 973 testing machine operating at a strain rate of 5×10^{-4} s^{-1} at room temperature. A 10 mm extensometer was used to accurately control and measure the displacement during tensile tests. The tensile testing was performed more than three times for each condition to verify the reproducibility.

The image acquisition system and post-processing system of digital image correlation (DIC) were performed utilizing Aramis 3.0 non-contact 3D strain measuring system developed by the GOM company. Before performing DIC measurement, a random pattern was created by spraying black paints on white background.

2.3. Microstructure characterization

Electron backscatter diffraction (EBSD), transmission electron microscopy (TEM), and three-dimensional atom probe tomography (3D-APT) were used to characterize the microstructures prior to and after tensile deformation. EBSD observations were performed utilizing a ZEISS Gemini 300 SEM with an EBSD detector. The minimum scanning step of 0.03 μm was used during the EBSD acquisition. The surfaces for EBSD observations were first grinded by sandpapers, and then polished by a 20 nm SiO_2 aqueous suspension. TEM and scanning TEM (STEM) observations were performed utilizing a JEOL-2100F at 200 kV. The element distributions were detected by energy dispersive spectroscopy (EDS) under STEM mode. The TEM samples were prepared and thinned by mechanically polishing first, followed by a twin-jet polishing using a solution of 5% perchloric acid and 95% ethanol at -40 °C and 65 V. Tip-shaped specimens for the 3D-APT tests were fabricated by a lift-out method and annularly milled by a focused ion beam/scanning electron microscope (FIB/SEM). The 3D-APT experiments were conducted utilizing a CAMECA LEAP 5000 XR instrument equipped with an ultraviolet laser with a spot size of 2 μm and a wavelength of 355 nm. The detection efficiency of this state-of-art microscope was about 52%. Data were acquired in the laser pulsing mode at a specimen temperature of 50 K with a target evaporation rate of 5 ions/1000 pulses, pulsing rate of 250 kHz, and laser pulse energy of 40 pJ. The APT data were reconstructed and analyzed using commercial IVAS 3.8.10 software.

3. Results and discussion

3.1. Outstanding tensile properties

Fig. 1(a) shows the tensile engineering stress-strain curves of the investigated MMS subjected to intercritical annealing at four different temperatures. For convenience, tensile specimens were denoted as “IA645”, “IA650”, “IA655” and “IA660”, respectively, based on intercritical annealing temperature. With decreasing intercritical annealing temperature, the yield stress (σ_{YS}), the uniform elongation (ε_{UE}), the tensile elongation (ε_{TE}), and the Lüders band strain (ε_{LB}) simultaneously increase. Moreover, the obvious serration phenomenon with large amplitudes is observed in the IA660 sample. Although the yield strength is substantially increased to GPa-level, the investigated MMS still has a remarkable ductility. The IA645 sample shows high yield strength beyond 1.1 GPa with excellent tensile uniform elongation over 50%, and the product of strength and elongation ($\sigma_{UTS} \times \varepsilon_{TE}$) also has an extremely high value (~70 GPa%) that is far beyond the indicator of third-generation AHSS (more than 30 GPa%). The synergy of strength and ductility for the developed MMS is much better than most high-performance steels, such as high-specific-strength steel (HSSS) [3,37], deformed and partitioned (D&P) steel [38], TWIP steel [39–42], and MMS [35,43,44], as shown in Fig. 1(b).

3.2. Initial microstructure with Mn heterogeneity and C segregation

Fig. 2(a) shows the EBSD phase map with grain boundaries for the IA650 sample, revealing a dual-phase of γ-austenite and α-ferrite with ultrafine grains. The volume fraction of austenite phase is about 43.8%, and the mean grain sizes of austenite and ferrite are about 331 and 378 nm, respectively. The volume fraction of austenite is measured based on large-area EBSD phase maps with more than 6000 grains. The ultrafine grain sizes for both phases

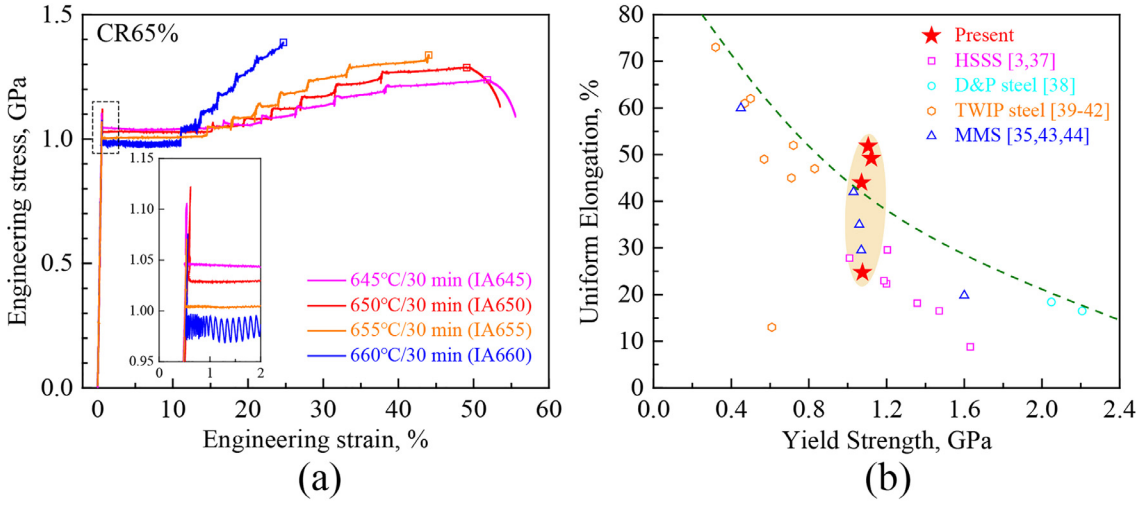

Fig. 1. Tensile properties of the investigated MMS after intercritical annealing at various temperatures. (a) Tensile engineering stress-strain curves. The corresponding ultimate strength points are marked by squares. The inset shows the close-up view of the yield point region. (b) Yield strength vs. uniform elongation for the investigated MMS, along with data for other high-performance steels [3,35,37–44].

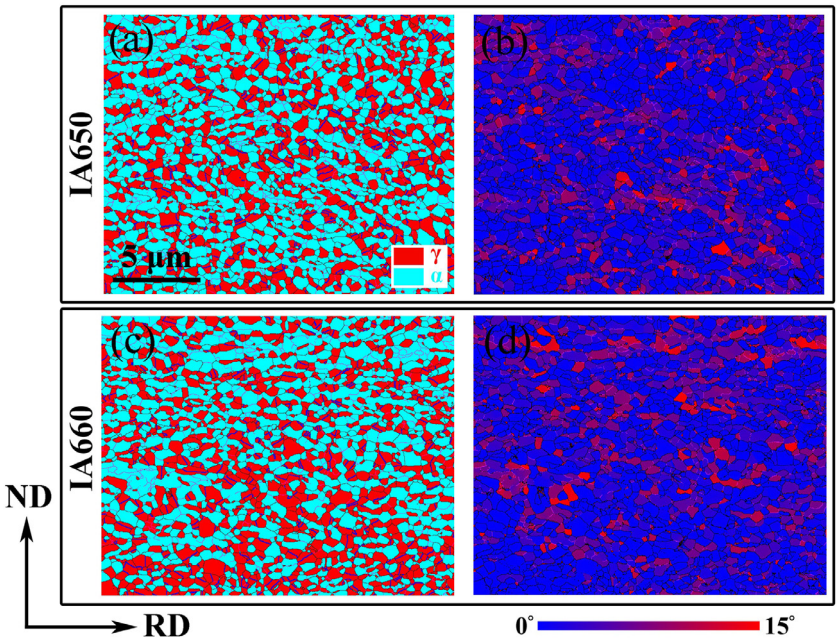

Fig. 2. Microstructures of the IA650 and IA660 samples prior to tensile testing. (a, b) EBSD phase map with grain boundaries and the GROD map for the IA650 sample. (c, d) EBSD phase map with grain boundaries and the GROD map for the IA660 sample. γ-austenite and α-ferrite are indicated by red region and cyan region, respectively and high-angle boundary ($\geq$ 15°), low-angle boundary (2°−15°), and twin boundary are denoted by black lines, fuchsia lines, and blue lines, respectively.

are one reason for the deficiency of initial mobile dislocations. Twin boundaries (TBs) are found in austenite grains and abundant low-angle boundaries (2°−15°) are observed in ferrite grains. The map of grain reference orientation deviation (GROD) for the IA650 sample is displayed in Fig. 2(b), indicating that most grains are recrystallized, the fully recrystallized ($\leq$ 5°) fractions of austenite and ferrite phases are about 92% and 71%, respectively [45]. The values of GROD greater than 5° are mainly existing in ferrite grains with low-angle boundaries. Microstructures of the IA660 sample are shown in Fig. 2(c) and (d), the volume fraction of austenite phase is about 48.8%, and the mean grain sizes of austenite and ferrite are about 397 and 485 nm, respectively. So the volume fraction of austenite and the mean grain sizes of both phases for the IA660 sample are larger than those for the IA650 sample. The fully recrystallized fractions of austenite and ferrite phases for the IA660 sample are about 91% and 66%, respectively.

The distributions of C, Mn, and Al atoms of the IA650 sample at the near-atomic scale were obtained by 3D-APT, as shown in Fig. 3(a) and (b). 3D-APT reveals significant C and Mn partitioning from ferrite to austenite [5,46], which results in a significant amount of retained austenite. C and Mn elements are enriched while the Al element is deprived in the austenite phase. The phase boundary is marked by a 6 at.% Mn iso-concentration surface and a peak distribution for the C atom. Such C segregation at phase boundaries can reduce the energy of phase boundaries, increase phase boundary cohesion, inhibit grain growth, and stabilize austenite, for elevating yield strength, and promoting discontinuous yielding [30,31].

Fig. 3(c) shows the STEM image of the IA650 sample prior to tensile testing, and the corresponding Mn distribution mapping is displayed in Fig. 3(d). The area with high concentration belongs to austenite phase since the Mn content in austenite is much higher

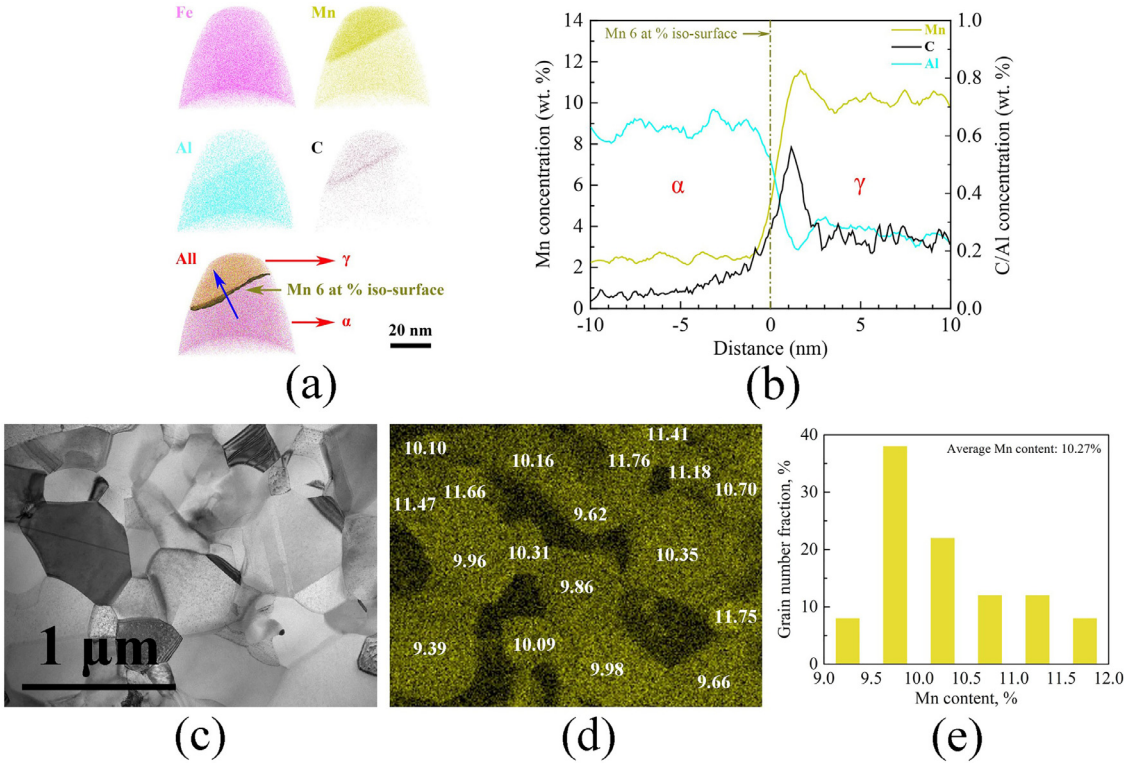

Fig. 3. Element distributions of the IA650 sample prior to tensile testing. (a, b) Near-atomic level chemical element distributions between γ and α, as revealed by 3D-APT. The phase boundary is marked by a 6 at.% Mn iso-concentration surface. (c, d) STEM image and the corresponding Mn distribution mapping. (e) Mn content distribution of various austenite grains.

than that in ferrite. The numbers inserted in Fig. 3(d) stand for the Mn content for each austenite grain. Moreover, the Mn content distributions of 50 austenite grains are counted and shown in Fig. 3(e), which indicates that the Mn distribution is slightly uneven in different austenite grains. For austenite phase, the Mn content range is from 9.39% to 11.76% and the average Mn content is 10.27%. The results of 3D-APT and STEM-EDS are consistent.

3.3. Heterogeneous deformation and non-uniform martensite transformation

The stress-strain curves (Fig. 1(a)) appear to be complete heterogeneous deformation features, which show a yield drop phenomenon followed by the onset of Lüders band and several PLC bands. It means that the investigated MMS has a strong deficiency of initial mobile dislocation.

In-situ full-field strain measurements by DIC during tensile tests and EBSD/TEM observations after each localized deformation band (LDB) passing through the entire gage length were used to investigate strain hardening mechanisms of heterogeneous deformation. The full-field strain distributions of the IA650 sample under various applied strains (ε_{app}) and distributions of axial strain (ε_L) at varying applied strains along axial position were displayed in Fig. 4. The fronts of localized deformation bands are closely perpendicular to the tensile axis and the local strain is observed to only increase within the localized deformation band. The deformation mode of the IA660 sample is similar to the IA650 sample, and the full-field strain distributions of the IA660 sample are displayed in Fig. 5. The observed PLC bands can be characterized as the type-A PLC bands since those PLC bands nucleate at one end of gage length and exhibit a continuous propagation feature [47].

When the applied stress reaches the upper yield stress, the Lüders band starts to nucleate at a weak point in the gage length area, resulting in a drop of the applied stress to the lower yield stress. During the Lüders band propagation, the plastic deformation is localized, and thus the macroscopic engineering stress is maintained almost constant until the band passes through the entire gage length. Schwab and Ruff [48] illustrated that the occurrence of a triaxial stress state can be developed at the yielded region within the band and the elastic region of the Lüders front. The Mises equivalent stress of the elastic region is higher than the applied stress, which will cause the elastic region to yield and push the propagation of the Lüders band. At the same time, the Mises equivalent stress of freshly yielded region resulting from elastic region will drop. The same principle should also be appropriate for the deformation of subsequent PLC bands. However, the regions where the localized deformation band develops and propagates need sufficient strain hardening capacity to counterbalance the force decrement due to the contraction of cross-sectional area, otherwise plastic instability would result in failure. In the present study, the grain sizes of investigated MMSs are extremely fine, which have insufficient strain hardening capacity in general [49,50].

Fig. 6(a) shows the change in volume fraction of austenite (V_γ) as a function of applied strain when several localized deformation bands pass through the entire gage length. The volume fraction of austenite is gradually reduced when each band propagates through, so martensite transformation plays an important role in localized bands and provides strain hardening for counterbalancing the force decrement due to the contraction of cross-sectional area. Moreover, the stepwise phase transformation in various grains might be attributed to the uneven Mn distribution in different austenite grains (Fig. 3), the martensite transformation should occur in the austenite grain with less Mn content. Fig. 6(b) shows the distributions for volume fraction of austenite along the axial direction in the IA650 sample prior to tensile testing and at an interrupted tensile strain of 8%. It is fascinating that the austenite essentially remains unchanged until the passage of the

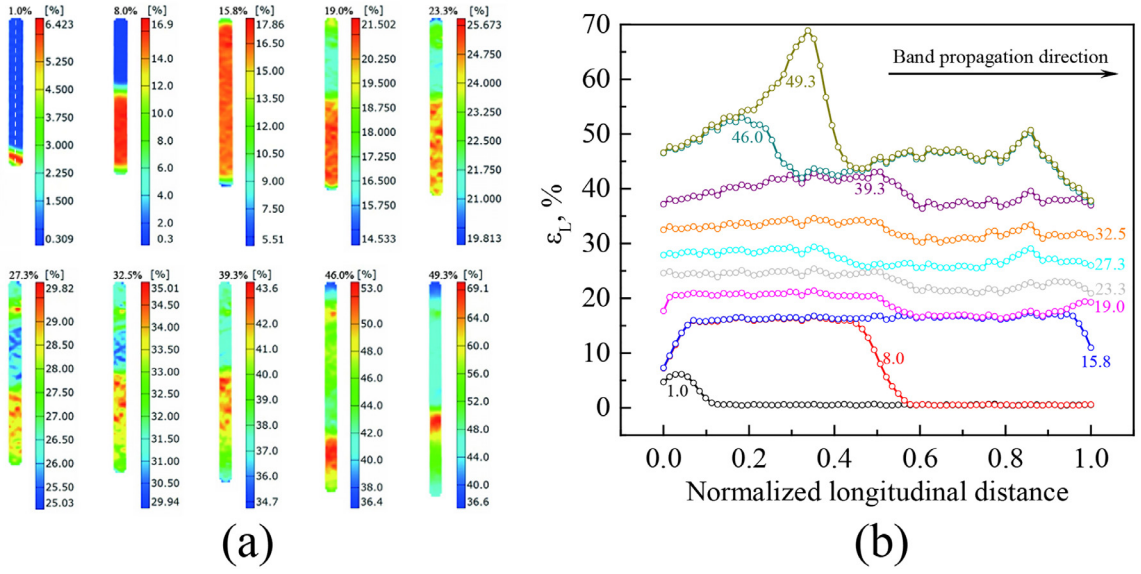

Fig. 4. Full-field strain distributions of the IA650 sample measured by DIC. (a) Contour maps of axial strain at various applied strains. Number above each map: ε_{app}. Color scale bar at the right ride for each map. (b) Distributions of ε_L along normalized axial position at varying applied strains, e.g. white vertical line in the first contour in (a).

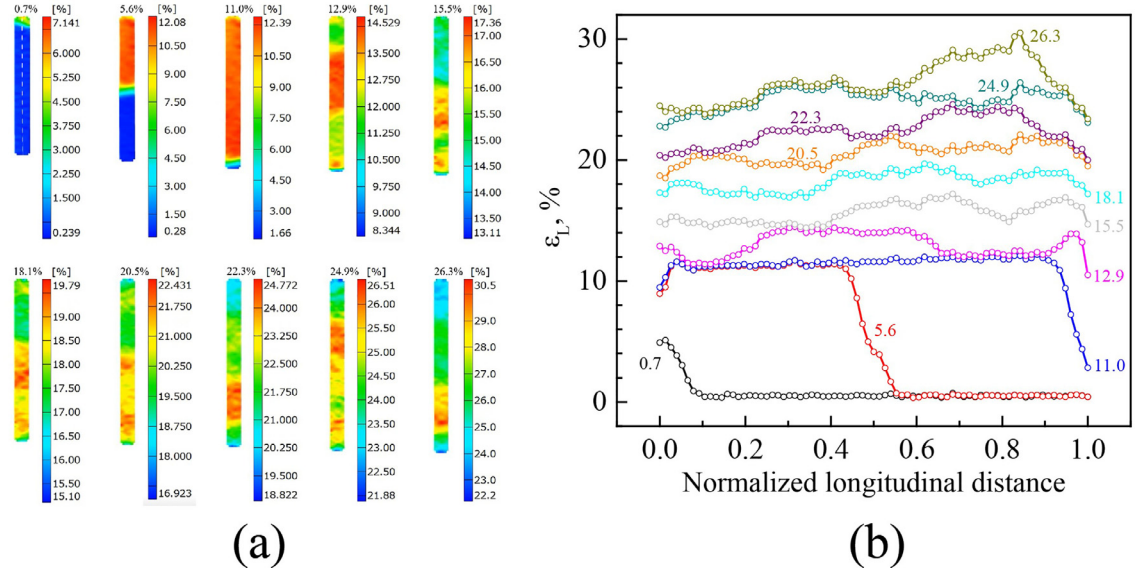

Fig. 5. Full-field strain distributions of the IA660 sample measured by DIC. (a) Contour maps of axial strain at various applied strains. (b) Distributions of ε_L along normalized axial position at varying applied strains.

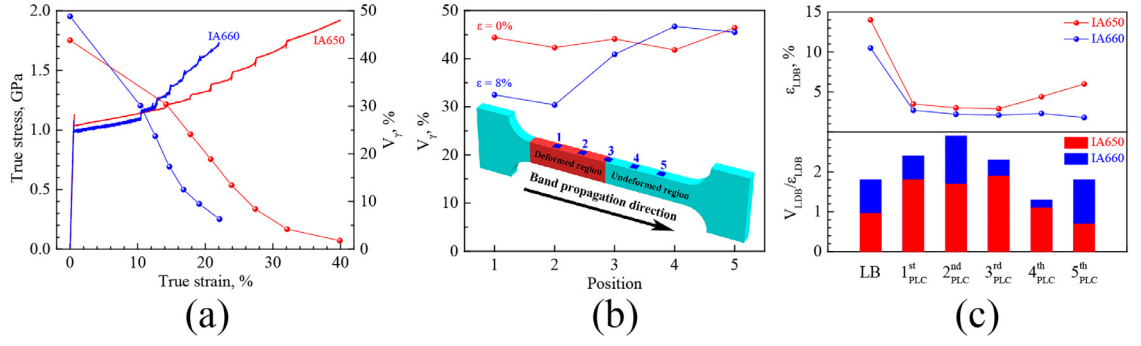

Fig. 6. (a) True stress-strain curves and volume fractions of austenite phase as a function of applied strain for both the IA650 and IA660 samples after several localized deformation bands pass through the entire gage length. (b) Distributions for volume fraction of austenite along the axial direction in the IA650 sample prior to tensile testing and at an interrupted tensile strain of 8%. The inset shows the schematic diagram of measuring positions. (c) Strain duration for each localized deformation band (ε_{LDB}) and normalized change of volume fraction of austenite by each ε_{LDB} ($V_{LDB}/\varepsilon_{LDB}$) for both the IA650 and IA660 samples.

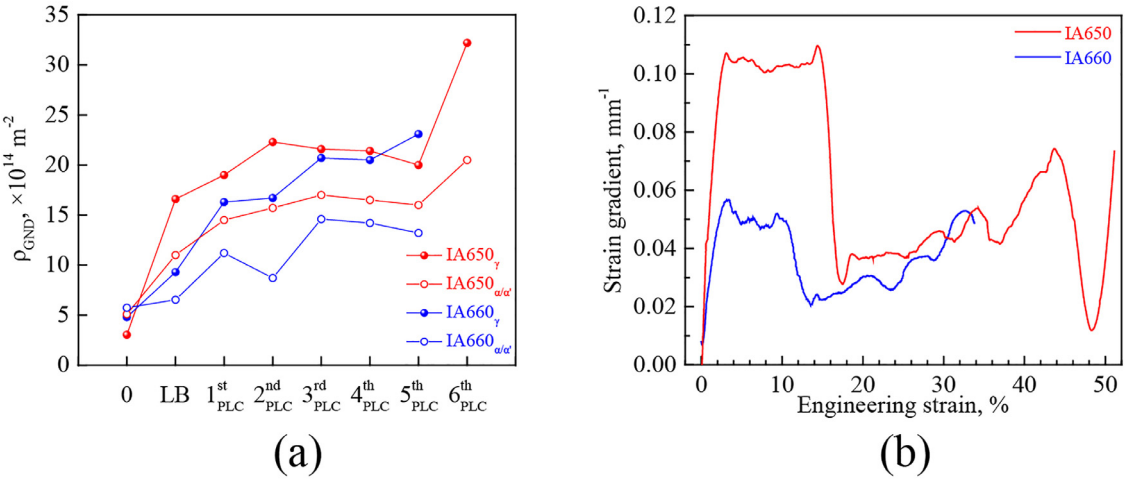

Fig. 7. (a) GND density evolutions of both the IA650 and IA660 samples after several localized deformation bands pass through the entire gage length. (b) Magnitudes of strain gradient at the front of localized deformation band as a function of applied strain for both the IA650 and IA660 samples.

band, indicating that the induced martensite transformation only occurs within the localized bands (Lüders band and PLC bands) [50]. The consumption rate of austenite phase for the IA660 sample is faster than the IA650 sample due to the more mechanically stable austenite grains for the IA650 sample [51]. The more stability for austenite grains in the IA650 sample can be attributed to the finer grains and more enrichment of austenite stabilizers [29]. The strain (ε_{LDB}) for each localized deformation band and the normalized change of volume fraction of austenite by ε_{LDB} ($V_{LDB}/\varepsilon_{LDB}$) are shown in Fig. 6(c). ε_{LDB} is higher while $V_{LDB}/\varepsilon_{LDB}$ is lower for the IA650 sample in all localized deformation bands, as compared to the IA660 sample. It indicates that the more stable austenite grains will result in a larger strain of localized deformation band by delaying the martensite transformation to a larger strain range, which leads to a significant improvement in the ductility. The residual volume fraction of austenite phase after the ultimate point for the IA650 sample is only about 1.8%, which indicates TRIP effect has been completely fulfilled for obtaining large ductility.

3.4. Strain gradient and heter-deformation-induced hardening

Although the engineering stress remains constant during the propagation of the Lüders band, the true stress still increases and the increment of true stress at the end of the Lüders band strain can be given by:

$$\Delta\sigma=\frac{F}{A_0}\varepsilon_{LB} \tag{1}$$

where F is the applied load, A_0 is the original cross-sectional area. The Lüders band strain of the IA650 sample (~16.4%) is larger than that of the IA660 sample (~11.5%) and the engineering stress (F/A_0) at the Lüders plateau of IA650 sample is also higher than that of the IA660 sample, in other words, the true stress increment of the IA650 sample is larger than that of the IA660 sample when the propagation of the Lüders band is over. On the one hand, the C content in the IA650 sample is slightly higher than that in the IA660 sample [29], resulting in slightly higher martensite strength for the IA650 sample. On the other hand, the amount of martensite transformation for the IA650 sample is smaller than that of the IA660 sample during the propagation process of the Lüders band (Fig. 6(a)). Besides the competition between these two factors, the other hardening sources (such as dislocation hardening) might also contribute to the strain hardening. The evolution of geometrically necessary dislocation (GND) density calculated by EBSD after several localized deformation bands passing through the entire gage length is shown in Fig. 7(a). The more stable austenite grains can accommodate a stronger dislocation multiplication capacity before martensite transformation. The higher magnitude of macroscopic strain gradients at the front of the Lüders band also needs more GNDs to accommodate for the IA650 sample, as shown in Fig. 7(b) [52–55]. The relation between GND density and strain gradient can be given by:

$$\rho_{GND}=\frac{1}{b}\frac{\partial\varepsilon}{\partial x} \tag{2}$$

where b is burgers vector. The strain gradient of the IA650 sample is larger than that of the IA660 sample, so the GND density of the IA650 sample should be larger than that of the IA660 sample for stronger hardening, which is consistent with results in Fig. 7(a). Besides the macroscopic strain gradients at the front of the Lüders band, the deformation incompatibility among different phases (austenite, ferrite and martensite) can also induce microscopic strain gradients at various phase boundaries [17]. These macroscopic and microscopic strain gradients would both account for strong heter-deformation-induced (HDI) hardening [45,56,57]. So the strain hardening difference between the IA650 and IA660 samples should be attributed to the overall competition among the amount of martensite transformation, the martensite strength, and the dislocation hardening.

3.5. High density of mobile dislocations by martensite transformation and DSA

Fig. 8 displays the TEM image of the IA650 sample at an interrupted strain of 27%. Abundant dislocations and stacking faults (SFs) are observed in austenite, and martensite transformation process is also discovered as shown in Fig. 8(a). Martensite transformation occurs in multiple regions of an individual austenite grain, and three indexed selected area diffraction (SAD) patterns (three circles with different colors are marked) with different orientations for α'-martensite phase are displayed in Fig. 8(a) with the electron beam closely parallel to the $[011]_\gamma$ zone axis. The corresponding SAD patterns of twins and stacking faults are also displayed in the insets of Fig. 8(a). Fig. 8(b) shows the dark-field image using the $(\bar{1}10)_{\alpha'}$ reflection in the indexed SAD pattern with the red frame, in which abundant dislocations are observed in martensite phase. High-density dislocations are also observed in ferrite, as shown in Fig. 8(c).

Fig. 9 shows the TEM image of the IA650 sample after ultimate strength point, in which abundant dislocations and stacking

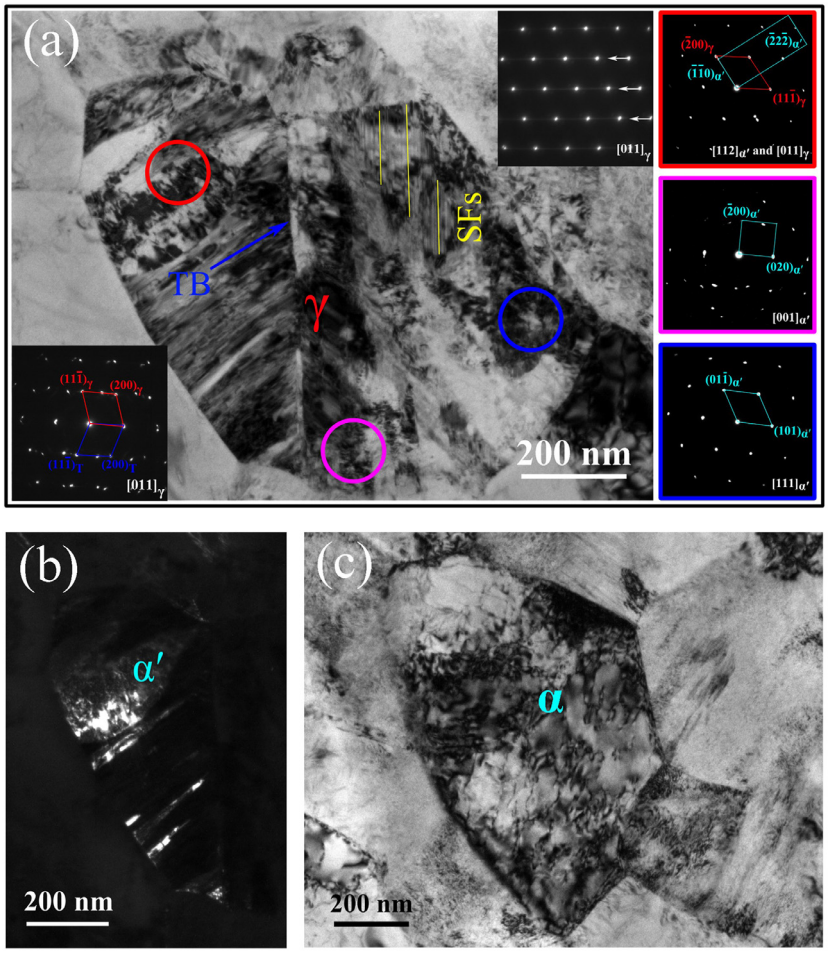

Fig. 8. TEM observations for the IA650 sample at an interrupted strain of 27%. (a) Martensite transformation process. (b) Dark-field image in (a). (c) Ferrite phase.

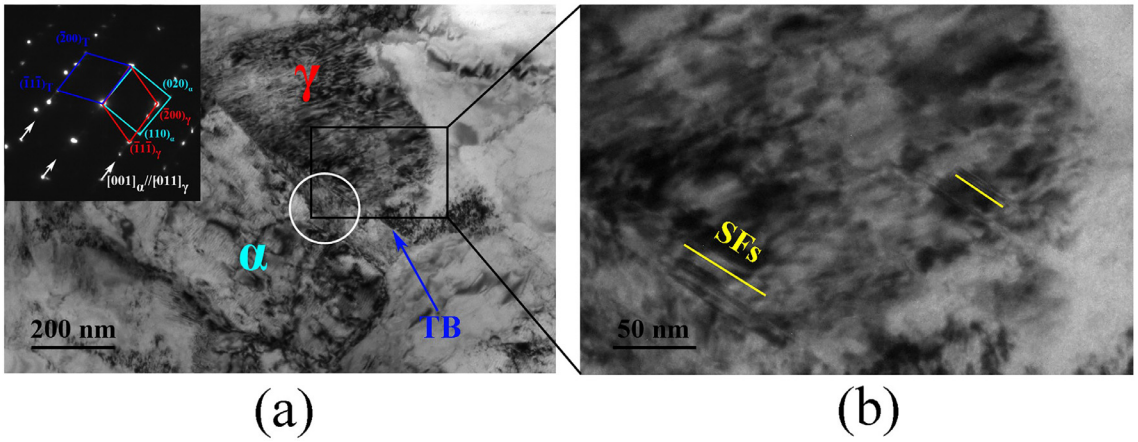

Fig. 9. TEM observations for the IA650 sample after ultimate strength point.

faults are also found in austenite phase and high-density dislocations are also observed in ferrite phase. The SAD pattern showing dual-phase, twins, and stacking faults is shown in the inset of Fig. 9(a). Therefore, massive dislocation multiplication occurs during deformation besides martensite transformation.

A general relationship between plastic strain and mobile dislocation density (ρ_m) can be written as [36]

$$\varepsilon = \rho_m bL/M \tag{3}$$

where L is the average glide distance of the mobile dislocation, M is the Taylor factor. Previous studies [38,58,59] have indicated that martensite formed by displacive shear transformation can induce an inherently high proportion (~18%) of mobile screw dislocations.

Carbon-dislocation interaction, which is regarded as the origin of DSA, can hinder the cross-slip of dislocations [60,61], resulting in a lower rate of dynamic recovery and therefore a higher rate of dislocation accumulation. Luo and Huang [62,63] illustrated that C atoms play a vital role in the accumulation of dislocations and therefore the strain-hardening rate of TWIP steels. High dislocation density induced by DSA is the dominant mechanism responsible for the high strain hardening rate of TWIP steels. Nam et al. [23] indicated that DSA occurring in the MMS can be explained

by the dislocation arrest model with long-range pipe diffusion of C atoms. Thus, the type-A serrations were proposed to be caused by DSA occurring in austenite. In the present study, C segregation at phase boundaries and enrichment in austenite grains (Fig. 2(d)) will result in strong DSA effect on promoting dislocation accumulation for high plastic deformation capacity. It is generally thought C segregation at phase boundaries can decrease the grain boundary energy and stabilize dislocation sources [64].

Mobile dislocations might be additionally pinned by the small martensite embryos until a higher stress is reached to unpin the dislocations [65]. The faster rate of martensite transformation will lead to more martensite embryos, which interact with mobile dislocations for higher serration amplitudes in the IA660 samples as compared to those for the IA650 sample.

In the deformation stage for PLC bands, the strain hardening rate of the IA660 sample is higher than that of the IA650 sample, as shown in Fig. 6(a). Firstly, the faster rate of martensite transformation provides stronger hardening for the IA660 sample. Secondly, the more martensite embryos result in a stronger DSA effect and HDI hardening for the IA660 sample. Lastly, the higher C content in austenite provides higher martensite strength, resulting in stronger hardening for the IA650 sample. In general, the first two factors are the main contributions for the strain hardening. However, the TRIP effect is consumed too fast due to the less stability for the austenite phase, and the average glide distance of the mobile dislocation is decreased quickly, resulting in reduced ductility for the IA660 sample.

4. Conclusions

In summary, we designed a new MMS exhibiting superior tensile properties. This MMS shows a yield strength beyond 1.1 GPa, a tensile uniform elongation over 50%, and a product of strength and elongation as high as about 70 GPa%, which is not accessible by the previously reported AHSS. The tensile behavior of this MMS shows a heterogeneous deformation feature, which displays a yield drop followed by a large Lüders band strain and several PLC bands. Multiple strain hardening mechanisms for the excellent tensile properties were revealed.

(1) Non-uniform martensite transformation is observed to only occur within localized deformation band. Initiation and propagation of every localized deformation band need a smaller amount of martensite transformation if austenite grains are more stable, and delay the martensite transformation to a larger strain range, which can lead to a significant improvement in the ductility. Suitable austenite stability by critical annealing can provide a persistent and complete TRIP effect during a large tensile strain range.
(2) High density of GNDs can be induced at the front of localized deformation band with a large macroscopic strain gradient and at various phase boundaries with a large microscopic strain gradient, resulting in strong HDI hardening. The more stable austenite grains can accommodate a stronger dislocation multiplication capacity before martensite transformation.
(3) Martensite transformation is generally formed by displacive shear transformation, which can generate an inherently high proportion of mobile screw dislocations. Moreover, interstitial C atoms were found to be segregated at phase boundaries and enriched in austenite, which can enhance the dislocation multiplication due to DSA effect. These two contributions provide high density of mobile dislocations for strong strain hardening.
(4) In general, the faster rate of martensite transformation provides stronger hardening and DSA effects, and results in a higher strain hardening rate. However, the TRIP effect is consumed too fast due to the less stability for the austenite phase, and the average glide distance of the mobile dislocation is decreased quickly, resulting in reduced ductility. Thus, more stable austenite grains and a lower rate of martensite transformation might be beneficial for large ductility, and C segregation at phase boundaries can decrease the grain boundary energy and stabilize dislocation sources that can promote dislocation multiplication, and the present findings should provide insights for composition design and tailoring microstructures for achieving excellent mechanical properties in AHSS.

Acknowledgments

This work is financially supported by the National Key R&D Program of China (No. 2017YFA0204402), the NSFC Basic Science Center Program for “Multiscale Problems in Nonlinear Mechanics” (No. 11988102), and the National Natural Science Foundation of China (Nos. 11790293 and 52192591).

References

[1] H. Aydin, E. Essadiqi, I.H. Jung, S. Yue, Mater. Sci. Eng. A 564 (2013) 501–508.
[2] O. Bouaziz, H. Zurob, M.X. Huang, Steel Res. Int. 84 (2013) 937–947.
[3] S.H. Kim, H. Kim, N.J. Kim, Nature 518 (2015) 77–79.
[4] R. Ding, Z.B. Dai, M.X. Huang, Z.G. Yang, C. Zhang, H. Chen, Acta Mater. 147 (2018) 59–69.
[5] Y.K. Lee, J. Han, Mater. Sci. Technol. 31 (2015) 843–856.
[6] H.P. Liu, H.E. Sun, B. Liu, D.Z. Li, F.G. Sun, X.J. Jin, Mater. Des. 83 (2015) 760–767.
[7] J. Jeon, S. Nam, S. Kang, J. Shin, H. Choi, Mater. Des. 92 (2016) 73–78.
[8] R.O. Ritchie, Nat. Mater. 10 (2011) 817–822.
[9] J.Y. He, H. Wang, H.L. Huang, X.D. Xu, M.W. Chen, Y. Wu, X.J. Liu, T.G. Nieh, K. An, Z.P. Lu, Acta Mater. 102 (2016) 187–196.
[10] T. Yang, Y.L. Zhao, Y. Tong, Z.B. Jiao, J. Wei, J.X. Cai, X.D. Han, D. Chen, A. Hu, J.J. Kai, K. Lu, Y. Liu, C.T. Liu, Science 362 (2018) 933–937.
[11] F.D. Fischer, G. Reisner, E. Werner, K. Tanaka, G. Cailletaud, T. Antretter, Int. J. Plast. 16 (2000) 723–748.
[12] B.C. De Cooman, O. Kwon, K.G. Chin, Mater. Sci. Technol. 28 (2012) 513–527.
[13] F. Yang, H. Luo, C. Hu, E. Pu, H. Dong, Mater. Sci. Eng. A 685 (2017) 115–122.
[14] H.W. Luo, J. Shi, C. Wang, W.Q. Cao, X.J. Sun, H. Dong, Acta Mater. 59 (2011) 4002–4014.
[15] D.P. Yang, P.J. Du, D. Wu, H.L. Yi, J. Mater. Sci. Technol. 75 (2021) 205–215.
[16] Y. Chang, C.Y. Wang, K.M. Zhao, H. Dong, J.W. Yan, Mater. Des. 94 (2016) 424–432.
[17] M.H. Zhang, H.Y. Chen, Y.K. Wang, S.J. Wang, R.G. Li, S.L. Li, Y.D. Wang, J. Mater. Sci. Technol. 35 (2019) 1779–1786.
[18] B. Hu, H.W. Luo, F. Yang, H. Dong, J. Mater. Sci. Technol. 33 (2017) 1457–1464.
[19] J. Han, S.J. Lee, J.G. Jung, Y.K. Lee, Acta Mater. 78 (2014) 369–377.
[20] H. Luo, H. Dong, M. Huang, Mater. Des. 83 (2015) 42–48.
[21] A.H. Cottrell, B.A. Bilby, Proc. Phys. Soc. Lond. Sect. A 62 (1949) 49–62.
[22] M.H. Zhang, L.F. Li, J. Ding, Q.B. Wu, Y.D. Wang, J. Almer, F.M. Guo, Y. Ren, Acta Mater. 141 (2017) 294–303.
[23] J.H. Nam, S.K. Oh, M.H. Park, Y.K. Lee, Acta Mater. 206 (2021) 116613.
[24] L. Chen, H.S. Kim, S.K. Kim, B.C. Cooman, ISIJ Int. 47 (2007) 1804–1812.
[25] H.F. Jiang, Q.C. Zhang, X.D. Chen, Z.J. Chen, Z.Y. Jiang, X.P. Wu, J.H. Fan, Acta Mater. 55 (2007) 2219–2228.
[26] A. Yilmaz, Sci. Technol. Adv. Mater. 12 (2011) 063001.
[27] P.G. Mccormick, Acta Metall. 36 (1988) 3061–3067.
[28] E. De Moor, D.K. Matlock, J.G. Speer, M.J. Merwin, Scr. Mater. 64 (2011) 185–188.
[29] S.J. Lee, S. Lee, B.C. De Cooman, Scr. Mater. 64 (2011) 649–652.
[30] B. Gao, Q.Q. Lai, Y. Cao, R. Hu, L.R. Xiao, Z.Y. Pan, N.N. Liang, Y.S. Li, G. Sha, M.P. Liu, H. Zhou, X.L. Wu, Y.T. Zhu, Sci. Adv. 6 (2020) eaba8169.
[31] Y. Ma, B.H. Sun, A. Schokel, W.W. Song, D. Ponge, D. Raabe, W. Bleck, Acta Mater. 200 (2020) 389–403.
[32] T. Bhattacharyya, S.B. Singh, S. Das, A. Haldar, D. Bhattacharjee, Mater. Sci. Eng. A 528 (2011) 2394–2400.
[33] D.W. Suh, S.J. Park, T.H. Lee, C.S. Oh, S.J. Kim, Metall. Mater. Trans. A 41 (2010) 397–408.
[34] B. Sun, F. Fazeli, C. Scott, S. Yue, Metall. Mater. Trans. A 47 (2016) 4869–4882.
[35] X. Zhang, R. Teng, T. Liu, Y. Shi, Z. Lv, Q. Zhou, X. Wang, Y. Wang, H. Liu, Z. Xing, Mater. Charact. 184 (2022) 111661.
[36] J.P. Hirth, J. Lothe, Theory of Dislocations, 2nd ed., Wiley, New York, 1982.
[37] Z.W. Wang, W.J. Lu, H. Zhao, C.H. Liebscher, J.Y. He, D. Ponge, D. Raabe, Z.M. Li, Sci. Adv. 6 (2020) eaba9543.
[38] B.B. He, B. Hu, H.W. Yen, G.J. Cheng, Z.K. Wang, H.W. Luo, M.X. Huang, Science 357 (2017) 1029–1032.
[39] J.H. Gao, S.H. Jiang, H.R. Zhang, Y.H. Huang, D.K. Guan, Y.D. Xu, S.K. Guan, L.A. Bendersky, A.V. Davydov, Y. Wu, H.H. Zhu, Y.D. Wang, Z.P. Lu, W.M. Rainforth, Nature 590 (2021) 262–267.
[40] R. Kalsar, S. Suwas, Scr. Mater. 154 (2018) 207–211.
[41] K.M. Rahman, V.A. Vorontsov, D. Dye, Acta Mater. 89 (2015) 247–257.

[42] Y.Z. Tian, Y. Bai, L.J. Zhao, S. Gao, H.K. Yang, A. Shibata, Z.F. Zhang, N. Tsuji, Mater. Charact. 126 (2017) 74–80.
[43] R. Ding, Y.J. Yao, B.H. Sun, G. Liu, J.G. He, T. Li, X.H. Wan, Z.B. Dai, D. Ponge, D. Raabe, C. Zhang, A. Godfrey, G. Miyamoto, T. Furuhara, Z.G. Yang, S. van der Zwaag, H. Chen, Sci. Adv. 6 (2020) eaay1430.
[44] L. Ma, T. Jia, G. Li, J. Hu, J.A. Jimenez, X. Gao, Mater. Sci. Eng. A 784 (2020) 139333.
[45] M.X. Yang, D.S. Yan, F.P. Yuan, P. Jiang, E. Ma, X.L. Wu, Proc. Natl. Acad. Sci. U. S. A. 115 (2018) 7224–7229.
[46] G. Miyamoto, A. Shibata, T. Maki, T. Furuhara, Acta Mater. 57 (2009) 1120–1131.
[47] M. Lebyodkin, L. Dunin-Barkowskii, Y. Brechet, Y. Estrin, L.P. Kubin, Acta Mater. 48 (2000) 2529–2541.
[48] R. Schwab, V. Ruff, Acta Mater. 61 (2013) 1798–1808.
[49] A.A. Howe, Mater. Sci. Technol. 16 (2000) 1264–1266.
[50] J.H. Ryu, J.I. Kim, H.S. Kim, C.S. Oh, H. Bhadeshia, D.W. Suh, Scr. Mater. 68 (2013) 933–936.
[51] Z.G. Xu, X. Shen, T. Allam, W.W. Song, W. Bleck, Mater. Sci. Eng. A 829 (2022) 142115.
[52] X.L. Wu, M.X. Yang, F.P. Yuan, G.L. Wu, Y.J. Wei, X.X. Huang, Y.T. Zhu, Proc. Natl. Acad. Sci. U. S. A. 112 (2015) 14501–14505.
[53] M.F. Ashby, Philos. Mag. 21 (1970) 399–424.
[54] H. Gao, Y. Huang, W.D. Nix, J.W. Hutchinson, J. Mech. Phys. Solids 47 (1999) 1239–1263.
[55] H.J. Gao, Y.G. Huang, Scr. Mater. 48 (2003) 113–118.
[56] Y.T. Zhu, X.L. Wu, Mater. Res. Lett. 7 (2019) 393–398.
[57] X.L. Wu, P. Jiang, L. Chen, F.P. Yuan, Y.T.T. Zhu, Proc. Natl. Acad. Sci. U. S. A. 111 (2014) 7197–7201.
[58] B.P.J. Sandvik, C.M. Wayman, Metall. Trans. A 14 (1983) 809–822.
[59] T.M. Hatem, M.A. Zikry, Mater. Sci. Technol. 27 (2011) 1570–1573.
[60] S.J. Lee, J. Kim, S.N. Kane, B.C. De Cooman, Acta Mater. 59 (2011) 6809–6819.
[61] V. Gerold, H.P. Karnthaler, Acta Metall. 37 (1989) 2177–2183.
[62] Z.C. Luo, M.X. Huang, Scr. Mater. 142 (2018) 28–31.
[63] Z.C. Luo, M.X. Huang, Scr. Mater. 178 (2020) 264–268.
[64] J.H. Kang, S. Duan, S.J. Kim, W. Bleck, Metall. Mater. Trans. A 47 (2016) 1918–1921.
[65] B.H. Sun, N. Vanderesse, F. Fazeli, C. Scott, J.Q. Chen, P. Bocher, M. Jahazi, S. Yue, Scr. Mater. 133 (2017) 9–13.